We are IntechOpen, the world's leading publisher of Open Access books Built by scientists, for scientists

4,800
Open access books available

122,000
International authors and editors

135M
Downloads

Our authors are among the

154
Countries delivered to

TOP 1%
most cited scientists

12.2%
Contributors from top 500 universities

WEB OF SCIENCE™

Selection of our books indexed in the Book Citation Index in Web of Science™ Core Collection (BKCI)

Interested in publishing with us?
Contact book.department@intechopen.com

Numbers displayed above are based on latest data collected.
For more information visit www.intechopen.com

Chapter 3

Numerical Simulations of Surface Plasmons Super-Resolution Focusing and Nano-Waveguiding

Xingyu Gao

Additional information is available at the end of the chapter

http://dx.doi.org/10.5772/50751

1. Introduction

Surface plasmons(SPs) are evanescent waves that propagate along the surface of dispersive media [1]. When a light beam incidents onto the surface of metal, the electromagnetic field interacts with the free electrons inside the metal, which leads to the oscillation of free electrons to excite the SPs in the exit medium. Noble metals with nanostructure geometry have special optical properties because they can excite localized surface plasmons (LSPs) under the illumination of light field. Since the pioneer study of Ritchie [2], the special optical properties of SPs in nano-scale have been tightly investigated. Various metallic nano-structures are reported for nano-plasmonic devices, including thin film[3,4], nanowires[5,6], nanorods[7,8], nano-hole array[9,10], nano-slits[11] et. al. Due to the sub-wavelength excitation range and strong field enhancement properties of SPs, they have been widely applied in super-resolution optical microscopy[12], nano-photonic trapping technology[13], biology and medical sciences[14] and nano-photonic waveguide[15].

In this chapter we firstly introduce a numerical algorithm for implementing the relative permittivity model of dispersive media in finite difference time domain(FDTD) method, i.e. piecewise linear recursive revolution(PLRC) method. Next the super-resolution phenomenon derived from the surface plasmons excited at the focal region is presented and analyzed. In the third part, we explore two kinds of plasmonic nano-waveguide: parallel nanorods and metal-dielectric-metal structure. Their optical properties, such as long distance waveguiding from the focal region, turning waveguiding effect and optical switch effect, will be demonstrated in detail. Finally, we conclude our research results in recent years and look forward the applications of surface plasmons in nano-technologies.

2. FDTD method for plasmonics simulation

The FDTD method was firstly proposed by Yee in 1966[16]. Because of its strong and precise power for simulating the propagation of the electromagnetic field, it was quickly applied in many research fields associate with the electromagnetics and optics. The detailed discrete differential equations of Maxwell equations can be found in Ref[17]. In this section, we mainly present the FDTD algorithm for dispersive media which is referred to as piecewise linear recursive revolution(PLRC) method and the verification of the program code.

2.1. 3D FDTD algorithm for dispersive media

The recursive revolution(RC) method for implementing the relative permittivity models of dispersive media in finite difference time domain(FDTD) algorithm was first proposed by Luebbers et al. [18] in 1990. It had been testified to perform faster calculation speed and fewer memory space requirement than the auxiliary differential equation(ADE) method [19], Z-transform method [20] and shift operator(SO) method [21]. In 1996, Kelley and Luebbers proposed the improved PLRC method [22] which remained the speed and low memory of RC method, and provided the accuracy existing in ADE method. The PLRC method for Drude model and Lorentz model has been presented respectively[22, 23]. In this section, we combine these two sets of formulations and propose the PLRC method for Drude-Lorentz model.

The curl equations of Maxwell's equations are presented as:

$$\nabla \times \mathbf{H} = \varepsilon \frac{\partial \mathbf{E}}{\partial t} \tag{1}$$

$$\nabla \times \mathbf{E} = -\mu \frac{\partial \mathbf{H}}{\partial t} \tag{2}$$

where **E** is the electric field vector and **H** is the magnetic field vector, respectively. ε and μ are the permittivity and permeability of the medium, respectively.

In dispersive medium, the displacement vector **D** has the linear relation with the electric field vector **E** in frequency domain as:

$$\mathbf{D}(\omega) = \varepsilon(\omega)\mathbf{E}(\omega) = \varepsilon_0 \varepsilon_r(\omega)\mathbf{E}(\omega) \tag{3}$$

where $\varepsilon_r(\omega)$ is the relative permittivity function of dispersive medium. It can be expressed by Drude-Lorentz model[24]as:

$$\varepsilon_r(\omega) = \varepsilon_\infty + \frac{\omega_d^2}{j\omega\gamma_d - \omega^2} + \frac{\Delta\varepsilon\omega_L^2}{\omega_L^2 + 2j\omega\delta_L - \omega^2} = \varepsilon_\infty + \chi_d(\omega) + \chi_L(\omega) \tag{4}$$

where ε_∞ is the relative permittivity at the infinite frequency, ω_d is the plasma frequency, γ_d is the oscillation rate of electrons, $\Delta\varepsilon$ is the difference of the relative permittivity between infinite frequency and zero frequency, ω_L is the oscillation rate of Lorentzian dipoles, δ_L is the decreasing coefficient, $\chi_d(\omega)$ and $\chi_L(\omega)$ are Drude susceptibility term and Lorentz susceptibility term respectively. The update equation for the electric field in FDTD format is:

$$\mathbf{E}^{n+1} = \left(\frac{\varepsilon_\infty - \xi^0}{\varepsilon_\infty - \xi^0 + \chi^0}\right)\mathbf{E}^n + \left(\frac{\Delta t/\varepsilon_\infty}{\varepsilon_\infty - \xi^0 + \chi^0}\right)\nabla \times \mathbf{H} + \left(\frac{1}{\varepsilon_\infty - \xi^0 + \chi^0}\right)\boldsymbol{\Psi}^n \tag{5}$$

where $\boldsymbol{\Psi}^n$ is an intermediary variable which includes the contributions from Drude term and Lorentz term, respectively. The parameters in Equ.(5) are combination of Drude and Lorentz terms. The contribution from Drude term for variable $\boldsymbol{\Psi}^n$ is updated as:

$$\boldsymbol{\Psi}_d^n = \left(\Delta\chi_d^n - \Delta\xi_d^n\right)\mathbf{E}^n + \Delta\xi_d^n\mathbf{E}^{n-1} + \boldsymbol{\Psi}^{n-1}\exp\left(-\gamma_d\Delta t\right) \tag{6}$$

where

$$\chi_d^n = \frac{\omega_d^2}{\gamma_d}\left[\Delta t - \frac{1}{\gamma_d}\left(1 - e^{-\gamma_d\Delta t}\right)\right] \tag{7}$$

$$\Delta\chi_d^n = -\frac{\omega_d^2}{\gamma_d^2}\left(1 - e^{-\gamma_d\Delta t}\right)^2 \tag{8}$$

$$\xi_d^n = \frac{\omega_d^2}{\gamma_d}\left[\frac{\Delta t}{2} - \frac{1}{\gamma_d^2}\left(1 - e^{-\gamma_d\Delta t}\right) + \frac{1}{\gamma_d}e^{-\gamma_d\Delta t}\right] \tag{9}$$

$$\Delta\xi_d^n = -\frac{\omega_d^2}{\gamma_d^2}\left[\frac{1}{\gamma_d\Delta t}\left(1 - e^{-\gamma_d\Delta t}\right)^2 - \left(1 - e^{-\gamma_d\Delta t}\right)e^{-\gamma_d\Delta t}\right] \tag{10}$$

The contribution from Lorentz term for variable $\boldsymbol{\Psi}^n$ is updated as:

$$\widehat{\boldsymbol{\Psi}}_L^n = \left(\Delta\hat{\chi}_L^n - \Delta\hat{\xi}_L^n\right)\mathbf{E}^n + \Delta\hat{\xi}_L^n\mathbf{E}^{n-1} + \widehat{\Psi}_L^{n-1}\exp\left((-\alpha + j\beta)\Delta t\right) \tag{11}$$

where "^" means it is a complex variable. $\alpha=\delta_L$, $\beta=(\omega_L^2-\delta_L^2)$, $\gamma = \Delta\varepsilon\omega_L^2$, and

$$\hat{\chi}_L^n = -\frac{j\gamma}{-\alpha+j\beta}\{1 - \exp[(-\alpha + j\beta)\Delta t]\} \tag{12}$$

$$\Delta\hat{\chi}_L^n = \frac{j\gamma}{-\alpha+j\beta}\{1 - \exp[(-\alpha + j\beta)\Delta t]\} \tag{13}$$

$$\hat{\xi}_L^n = \frac{j\gamma}{\Delta t(\alpha-j\beta)^2}\{[(\alpha - j\beta)\Delta t + 1]\exp[(-\alpha + j\beta)\Delta t] - 1\} \tag{14}$$

$$\Delta\hat{\xi}_L^n = \frac{j\gamma}{\Delta t(\alpha-j\beta)^2}\{[(\alpha - j\beta)\Delta t + 1]\exp[(-\alpha + j\beta)\Delta t] - 1\}\{1 - \exp[(-\alpha + j\beta)\Delta t]\} \tag{15}$$

Finally the variable $\boldsymbol{\Psi}^n$ is the sum of Drude term and the real part of Lorentz term:

$$\boldsymbol{\Psi}^{\mathbf{n}} = \boldsymbol{\Psi}_d^n + \mathrm{Re}\left(\widehat{\boldsymbol{\Psi}}_L^n\right) \tag{16}$$

The parameters in Equ.(5) are also the sum of Drude term and the real part of Lorentz term:

$$\chi^{\mathbf{n}} = \chi_d^n + \mathrm{Re}\left(\hat{\chi}_L^n\right) \tag{17}$$

$$\xi^{\mathbf{n}} = \xi_d^n + \mathrm{Re}\left(\hat{\xi}_L^n\right) \tag{18}$$

From above equations we can see that the Drude and Lorentz terms are deduced respectively, so that the PLRC method can be applied for both Drude and Drude-Lorentz

models. For describing the relative permittivity of silver[25], we adopt the values of the parameters of Drude-Lorentz model as ε_∞=4.6, ω_d=1.401×10^{16}Hz, γ_d=4.5371×10^{13}Hz, $\Delta\varepsilon$=3.428, ω_L=2.144×10^{16}Hz, and δ_L=1.824×10^{18}Hz.

2.2. Verification of the program code

We adopt the classical Krestschmann-Type SPR device shown in Fig.1(a) to verify our FDTD code. The two-dimensional(2D) simulation conditions are: n_1=1.78, n_2=1.132, θ=42º, thickness of silver film d=50nm, and sampling interval Δx=Δy=5nm. Under these configurations, the SPR wavelength calculated by SPs dispersion relation is λ_{SP}=500nm. A modulated 2D TE Gaussian pulse with the central wavelength 400nm is incident from the medium n_1 onto the metal film. The transmission enhancement coefficients in the visible range in the medium n_2 calculated by ADE, SO and PLRC methods are shown in Fig.1(b). These three methods demonstrate the same SPR peak and enhancement strength under the same condition. However, in the shorter wavelength region the ADE method shows larger error, and in the longer wavelength region the SO method shows larger error. So in the total wavelength region, the PRLC method shows better precision than those two methods. We will use the PLRC method and the parameters of Drude-Lorentz model mentioned above throughout this chapter.

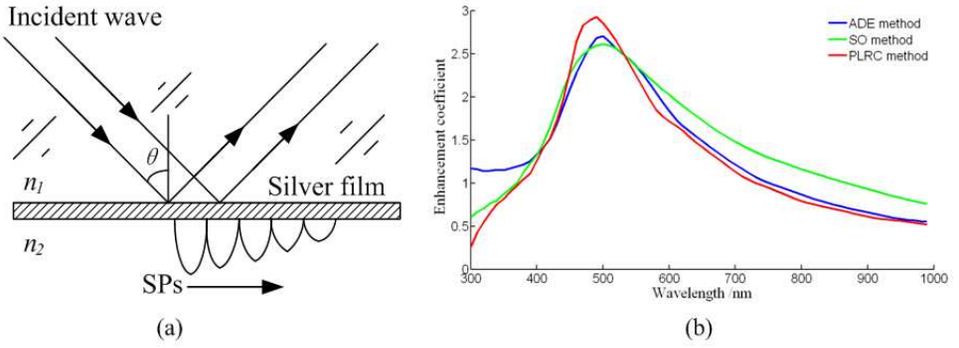

Figure 1. Verification of our FDTD code for dispersive media. (a) Configuration of Krestschmann-Type SPR device; (b) Compare of the enhancement coefficients of the three methods.

3. Application of surface plasmons in super-resolution focusing

A tightly focused evanescent field can be generated by a centrally obstructed high numerical aperture objective lens [26], and a super-resolved evanescent focal spot of λ/3 has been obtained [27]. The enhancement of the electromagnetic (EM) field by tight focusing enables nano-lithography using evanescent field [28]. It has been demonstrated that a tightly focused beam can be further modulated by a negative-refraction layer together with a nonlinear layer [29] or a saturable absorber [30] to approximately λ/4~λ/5 close vicinity of the focus. Considering the difficulty in realizing a negative-refraction layer in practice, here we introduce another mechanism of light modulation in the tightly focused region. Due to the use of high numerical aperture objective lens, the focused evanescent field is highly depolarized, which offers strong transverse and longitudinal polarization components.

Therefore the deployment of nano-plasmonic structure, which is polarization sensitive, offers new mechanism to modulate the focused evanescent field. In this section, we will give two research results for the application of surface plasmons in super-resolution focusing.

3.1. Simulation of radially polarized focusing through metallic thin film

As shown in Fig.2, the configuration of tightly focused evanescent field is based on the scanning total internal reflection microscopy[26]. The refractive indices of immersion oil and the coverslip glass are 1.78. The thin silver film is coated on the surface of the coverslip glass. An annular radially polarized incident beam is focused on the upper surface of coverslip glass by an objective. We define the annular coefficient ε=d/D which produces a ring beam illumination onto the silver film. In the simulation we set ε=0.606 to make sure that the incident angle is larger than the critical angle for the total internal reflection of the ring beam.

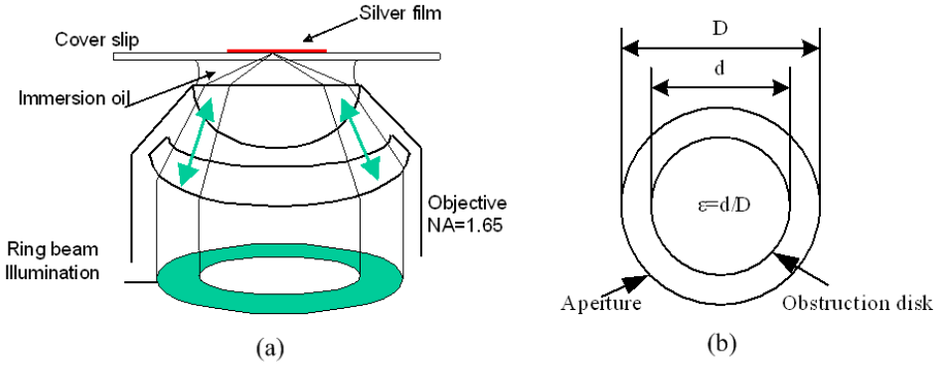

Figure 2. The configuration of focal ring beam illumination for the excitation of SPs. (a) Scheme of total internal reflection focusing; (b) Illustration of annular coefficient.

The electromagnetic field of radially polarized focal beam is expressed as:

$$\mathbf{E}(\mathrm{r}, \boldsymbol{\Psi}, \mathrm{z}) = \mathrm{i}k(cos\Psi \boldsymbol{I}_1 \mathbf{i} + sin\Psi \boldsymbol{I}_1 \mathbf{i} + \boldsymbol{I}_0 \mathbf{K}) \tag{19}$$

where

$$\boldsymbol{I}_0 = \int_0^{\alpha} \sqrt{\cos\theta}\, \sin^2\theta J_0(krsin\theta) exp(-ikzcos\theta) d\theta \tag{20}$$

$$\boldsymbol{I}_1 = \int_0^{\alpha} \sqrt{\cos\theta}\, \sin\theta cos\theta J_1(-krsin\theta) exp(-ikzcos\theta) d\theta \tag{21}$$

where **i**, **j** and **k** are unit vectors in the x, y and z directions, respectively. $\mathrm{r} = \sqrt{\mathrm{x}^2 + \mathrm{y}^2}$ is transverse radial coordinate. Ψ denotes the angle between r and $+x$ axis. θ denotes the incident angle of light. $J_i(x)$ is the ith order Bessel function of the first kind. It should be pointed out that the electric fields under the radially polarized focal beam is circular symmetrical. The simulation conditions are set as: incident wavelength λ=532nm, NA=1.65, sampling interval Δx=Δy=Δz=5nm, thickness of silver film d=60nm. In this simulation, we calculate the electric field in the transverse plane with the defocal distance z=-600nm as the input source.

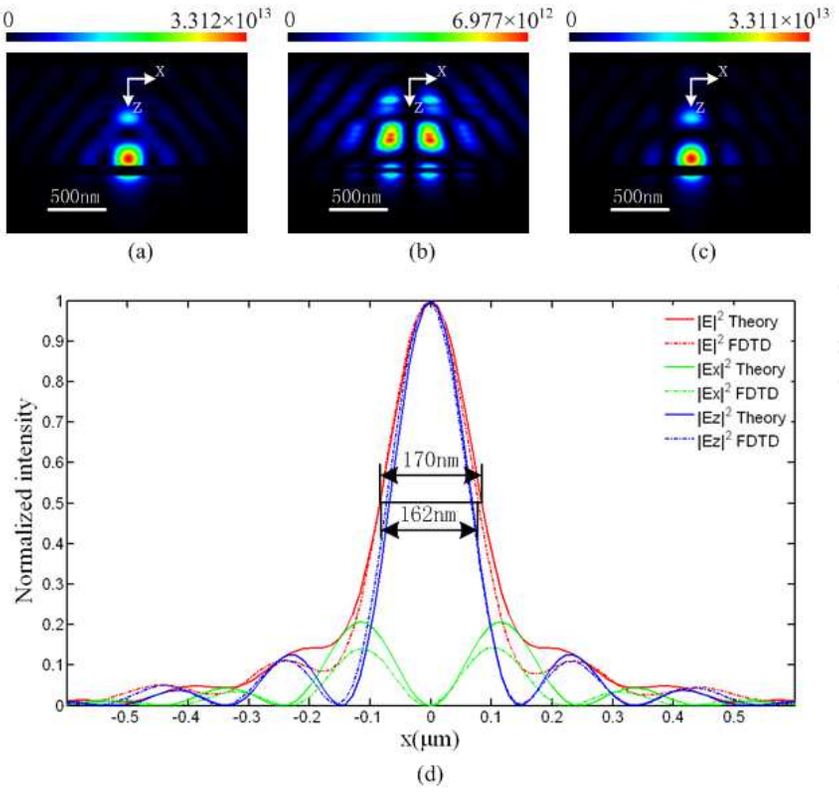

Figure 3. The intensity distribution of radially polarized beam focusing through silver film. Colorbar unit: V^2/m^2. (a) $|E_{total}|^2$; (b) $|E_x|^2$; (c)$|E_z|^2$; (d)Comparison of the sizes of the SPs enhanced focus with that of theoretical normal focus.

Under the conditions mentioned above, after 2000 time steps simulation, the time averaged intensity distributions of E_{total}, E_x and E_z in xz plane are shown in Fig.3. The intensity of total electric field is the combination of E_x and E_z components. The E_z field shows a single evanescent focus which is formed by the SPs excited by the silver film and the total electric field is dominated by E_x component. In order to illustrate the super-resolved SPs focus phenomenon, we plot the SPs focus simulated by FDTD and the theoretical radially polarized focus calculated by Debye theory along x axis in Fig.3(d). The intensity distributions of the SPs focus and the theoretical focus are normalized by the maximum values of their total electric fields. It is demonstrated that the proportion of E_x intensity and Ex intensity of SPs focus is 0.145, while that of the theoretical focus is 0.207, which indicates that the E_z component is enhanced by the SPs. So that the focal size of SPs enhanced focus(FWHM=162nm) is smaller than that of the theoretical focus(FWHM=170nm).

It is obviously that in the total electric field distribution, the reflected field is much stronger than the transmitted field. Under the annular coefficient $0.606<\varepsilon<1.0$ condition, the total ring beam includes a wide range of incident angle($34.18^o< \theta<67.97^o$). However, only the narrow angle ranges around $\theta=36.72°$ satisfy the SPs dispersion relation. We simulate the thin ring beam illumination ($0.645<\varepsilon<0.65$) which contains the SPR incident angle and the thin ring beam illumination ($0.795<\varepsilon<0.8$) which is far from the SPR incident angle in order to demonstrate the differences between the SPR focus and non-SPR focus.

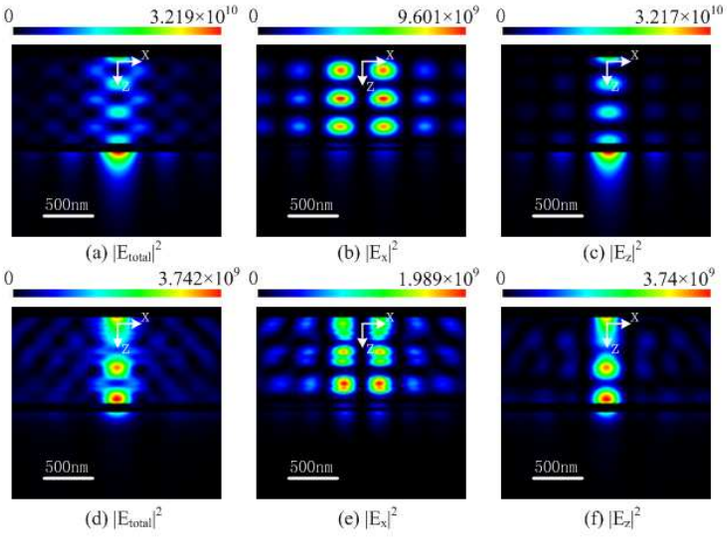

Figure 4. The intensity distributions of SPR focus (a), (b), (c) and non-SPR focus (d), (e), (f) in xz plane. Colorbar unit: V^2/m^2.

The simulation results are shown in Fig.4. Comparing Fig.4(a) and (d), it can be seen that under the SPs dispersion relation, the SPR significantly enhances the focus below the silver film, which leads to a much high transmission rate of the focal field. While for the non-SPR focus, the reflection is much stronger than the transmission, so most part of the focus energy is reflected back. Comparing the E_x components of the two conditions in Fig.4(b) and (e), they demonstrate almost the same distribution with no SPR phenomenon. That is because the E_x component is parallel to the silver film, i.e. s-polarization, it can't excite the SPR. Finally, comparing the E_z components that are perpendicular to the silver film, i.e. p-polarization, of the two conditions in Fig.4(c) and (f), it is obviously demonstrated that the E_z component contributes to the SPR focus dominantly. For the SPR focus, the E_z component is significantly enhanced by the SPR, while for the non-SPR focus, the reflection of E_z component is much larger than its transmission. The SPs dispersion relation satisfied by the ring beam with $0.645<\varepsilon<0.65$ is the main mechanism for the super-resolved SPs focus. This phenomenon gives rise to a simple approach for achieving a super-resolution focus beyond diffraction limit, which has potential applications in nano-lithography and nano-trapping.

3.2. Simulation of focusing through two parallel nanorods

3.2.1. Numerical simulation model

Our simulation configuration is shown in Fig.5. Two silver nanorods are lying on the interface of two dielectric media with the separation (D) of 120nm centre-to-centre. The refractive index of lower medium (n_1) is 1.78 and the refractive index of upper medium (n_2) is 1.0. The size of the nanorods is 150nm in length (l) and 50nm in diameter (d). The numerical aperture of the objective is 1.65, and the pure focused evanescent field is generated by inserting a centrally placed obstruction with normalized radius ε_c=0.606, corresponding to the total internal refraction condition.

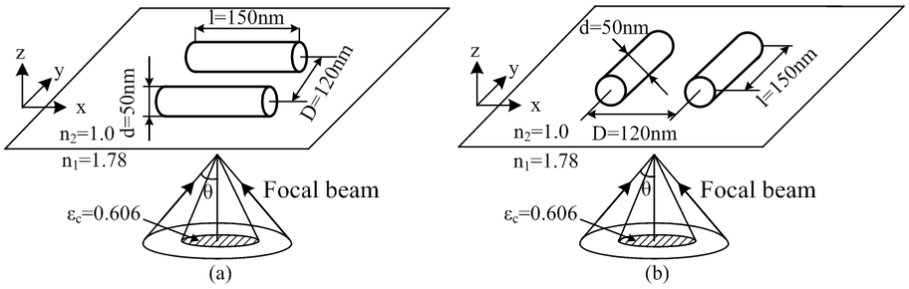

Figure 5. Configuration of nano-plasmonic waveguide. (a) Nanorods lie along x direction. (b) Nanorods lie along y direction.

If the illuminating beam polarizes along the *x* direction, the electric field at the focal region, calculated with high angle vectorial Debye theory, is highly depolarized, and each polarization component can be expressed as:

$$\mathbf{E}(\mathrm{r},\boldsymbol{\Psi},\mathrm{z}) = \frac{\pi \mathrm{i}}{\lambda}\{[\boldsymbol{I}_0 + \cos(2\Psi)\boldsymbol{I}_2]\mathbf{i} + \sin(2\Psi)\boldsymbol{I}_2\mathbf{J} + 2\mathrm{i}\cos(2\boldsymbol{\Psi})\boldsymbol{I}_1\mathbf{K}\} \tag{22}$$

where

$$\boldsymbol{I}_0 = \int_0^{\alpha}\sqrt{\cos\theta}\,\sin\theta(1+cos\theta)J_0(krsin\theta)exp(-ikzcos\theta)d\theta \tag{23}$$

$$\boldsymbol{I}_1 = \int_0^{\alpha}\sqrt{\cos\theta}\,\sin^2\theta J_1(-krsin\theta)exp(-ikzcos\theta)d\theta \tag{24}$$

$$\boldsymbol{I}_2 = \int_0^{\alpha}\sqrt{\cos\theta}\,\sin\theta(1-cos\theta)J_2(krsin\theta)exp(-ikzcos\theta)d\theta \tag{25}$$

where **i**, **j** and **k** are unit vectors in the *x*, *y* and *z* directions, respectively. $\mathrm{r} = \sqrt{\mathrm{x}^2+\mathrm{y}^2}$ is transverse radial coordinate. Ψ denotes the angle between *r* and +*x* axis. *θ* denotes the incident angle of light. $J_i(\mathrm{x})$ is the *i*th order Bessel function of the first kind. The electric and magnetic fields are calculated at a plane one wavelength before the interface as the input source for the FDTD simulation. The total field/scatter field technique is used to eliminate the light propagating to –z direction, so that the incident focal beam only propagates in forward direction.

In the simulation, the wavelength of incident focal beam is 532*nm*. It should be noted that the annular beam illumination includes a wide range of incident angle (34.18°<θ<69.97°), which corresponds to a wide range of surface plasmon resonance (SPR) wavelengths (340*nm*<*λ*<1120*nm*). Our simulations show that different wavelengths selected in this spectrum range make little difference for the excitation of LSPs by the nano-plasmonic waveguide. The grid sizes Δ*x*, Δ*y* and Δ*z* for each dimension are set to 2.34*nm*. According to the discretization in space domain, the discretization in time domain that satisfies the Courant stability condition is adopted as:

$$\Delta\mathrm{t} = \frac{0.985}{\mathrm{c}\sqrt{1/\Delta\mathrm{x}^2+1/\Delta\mathrm{y}^2+1/\Delta\mathrm{z}^2}} \tag{26}$$

where *c* is the velocity of light in vacuum. Under these configurations, the iteration of program runs 400 time steps for a period. In order to obtain the stable state of the optical field, 10 periods are adopted, i.e. 4000 time steps are calculated in the simulation.

3.2.2. Simulation results and discussion

The intensity distribution of a focused evanescent field under the linearly polarized illumination is shown in Fig.6 and agrees well with previous theory[26, 27]. Under the conditions described above, the intensity of E_y component is one order smaller than either E_x or E_z, so the overall impact of E_y on the intensity distribution is less significant. Due to the depolarization effect, a strong longitudinal E_z component appears, with its strength comparable to the illuminating polarization component E_x, i.e., $|E_z|^2/|E_x|^2 \approx 0.85$. As a result, the intensity distribution of the total field is splitted to two lobes shown in Fig.6 (a).

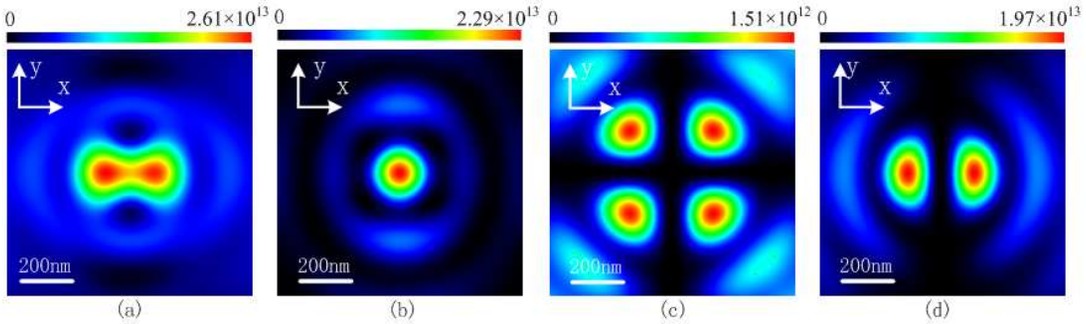

Figure 6. The intensity distribution of evanescent electric field for linearly polarized focal beam at the interface. (a) $I=|E_x|^2+|E_y|^2+|E_z|^2$ (b) $|E_x|^2$ (c) $|E_y|^2$ (d) $|E_z|^2$ (Unit: V^2/m^2)

The modulation of the focused evanescent field by a pair of silver nanorods is demonstrated in Fig. 7, where the intensity distributions in planes of different distances from the interface are illustrated. In the left column, when there is no nanorod on the interface, the focal spot splits into two lobes at different distances above the interface. In the middle column, the nanorods are lying along *x* direction, parallel to the dominant transverse polarization component E_x. In the right column, the nanorods are lying along *y* axis, perpendicular to the dominant transverse polarization component E_x. In Fig.7 (a), it is noted that at the *xy* plane 25*nm* above the interface, the electric field is significantly enhanced by the LSPs between the nanorods, if the nanorods are lying in the *y* direction, resulting in a strong localized field between the two nanorods. While the nanorods are lying in the *x* direction, the electric field shows less enhancement and localization. At the plane 60*nm* above the interface (10*nm* above the nanorods, Fig.7 (b)), it is observed that the longitudinal electric field component E_z displays a strong enhancement at both ends of each nanorod, forming four strong intensity lobes. When the nanorods are lying along *x* direction, the dominant transverse electric field component E_x is not significantly enhanced, so the electric field is dominated by the longitudinal component E_z, which shows four strong intensity lobes. However when the nanorods lie in the *y* direction, due to the significant enhancement of E_x component between the nanorods, the four strong lobes become less evident. At the horizontal planes that further away from the nanorods, i.e. at the planes 75*nm* (Fig.7 (c)) and 100*nm* (Fig.7 (d)) above the interface, super-resolved focal spots are demonstrated. In particular, with the significant enhancement of dominant transverse electric field component E_x, the focal spots show narrower distribution and stronger strength, when the nanorods lie in the direction perpendicular to the E_x component.

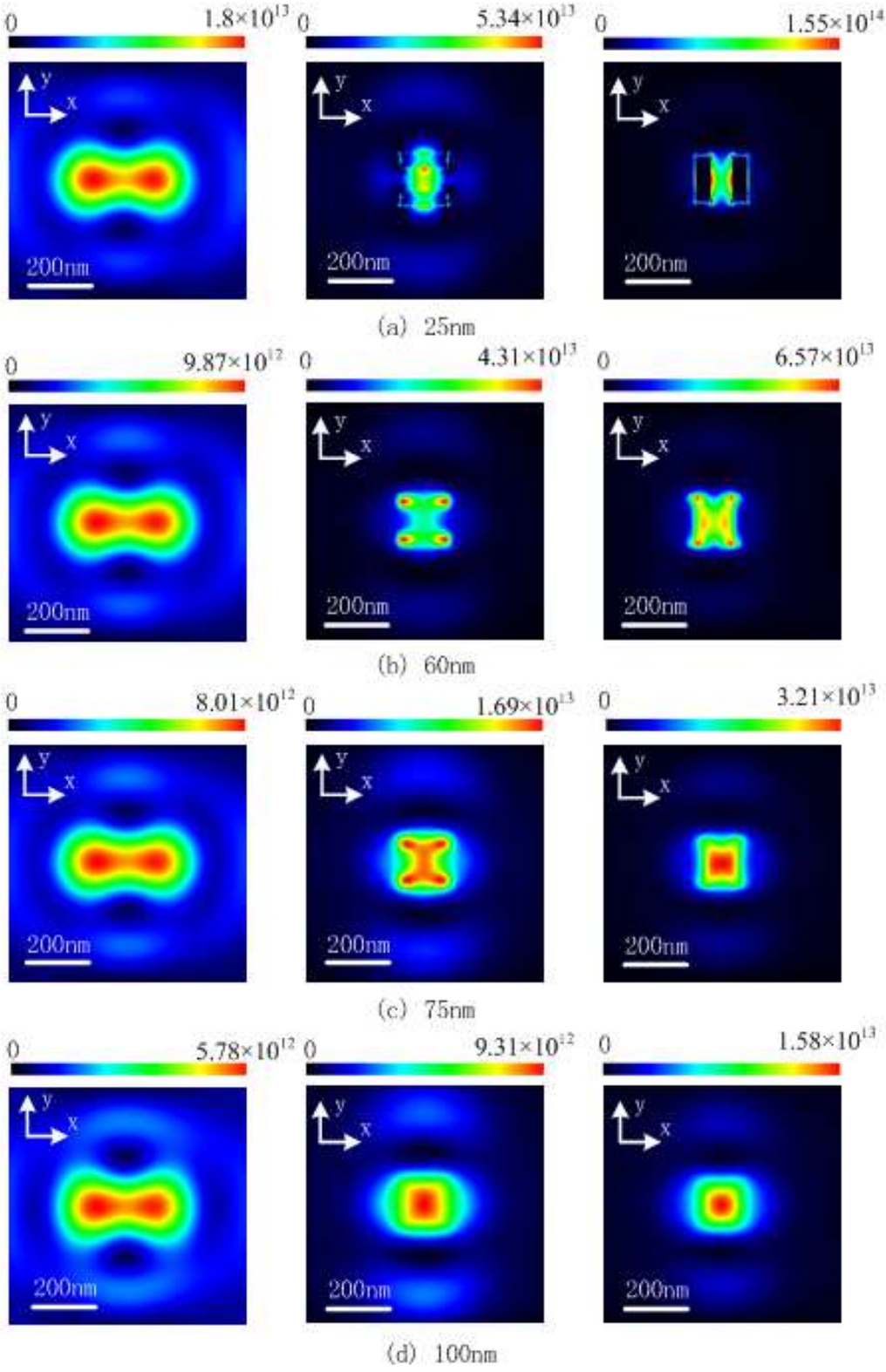

Figure 7. Intensity distributions for linearly polarized focal beam in *xy* plane of different distances from the interface. In the left column there is no nanorod. In the middle column the nanorods are lying along x direction. In the right column the nanorods are lying along y direction. (Unit: V^2/m^2)

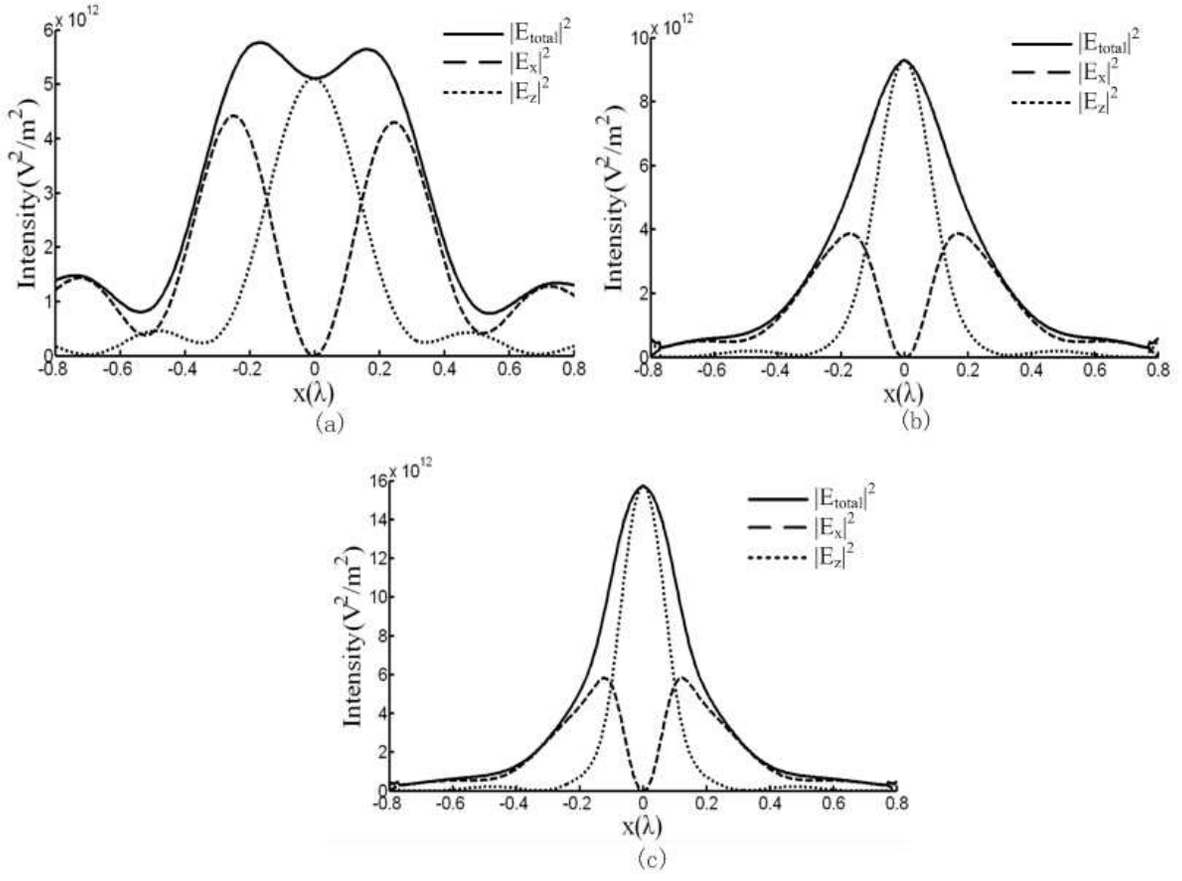

Figure 8. Cross sections for polarization components of linearly polarized light along x axis at the xy plane 100nm above the interface. (a) Without nanorods; (b) Nanorods lie along x direction; (c) Nanorods lie along y direction.

The detailed analysis of the LSPs effect on each polarization component at the plane 100*nm* above the interface is illustrated in Fig.8. When the nanorods are lying along x direction (Fig. 8(b)), the enhancement of E_z component is insignificant compared with the case that the nanorods lie in the *y* direction. Nevertheless, it still produces a narrower focal spot with 46.6% reduction in FWHM and 61% increase in strength. When the nanorods are lying in *y* direction (Fig. 4(c)), the dominant transverse polarization E_z is not only significantly enhanced in strength, e.g. by a factor of 2.71, but also becomes more localized, e.g. the full width at half maximum (FWHM) is reduced from 388*nm* to 149*nm*. This phenomenon indicates the LSPs excited by the E_z component couple between the nanorods and re-distribute the energy of electromagnetic field. The longitudinal component E_z is also enhanced by a factor of 1.4, and becomes narrower, e.g. the distances between two intensity peaks reduced from 266*nm* to 127*nm*. As a result, a super-resolution focal spot can be formed outside the waveguide. The above analysis shows that the nano-plasmonic waveguide provides strongest enhancement to the transverse polarization component perpendicular to the nanorods, followed by the longitudinal polarization component, and the enhancement for the transverse polarization component parallel to the nanorods is least significant.

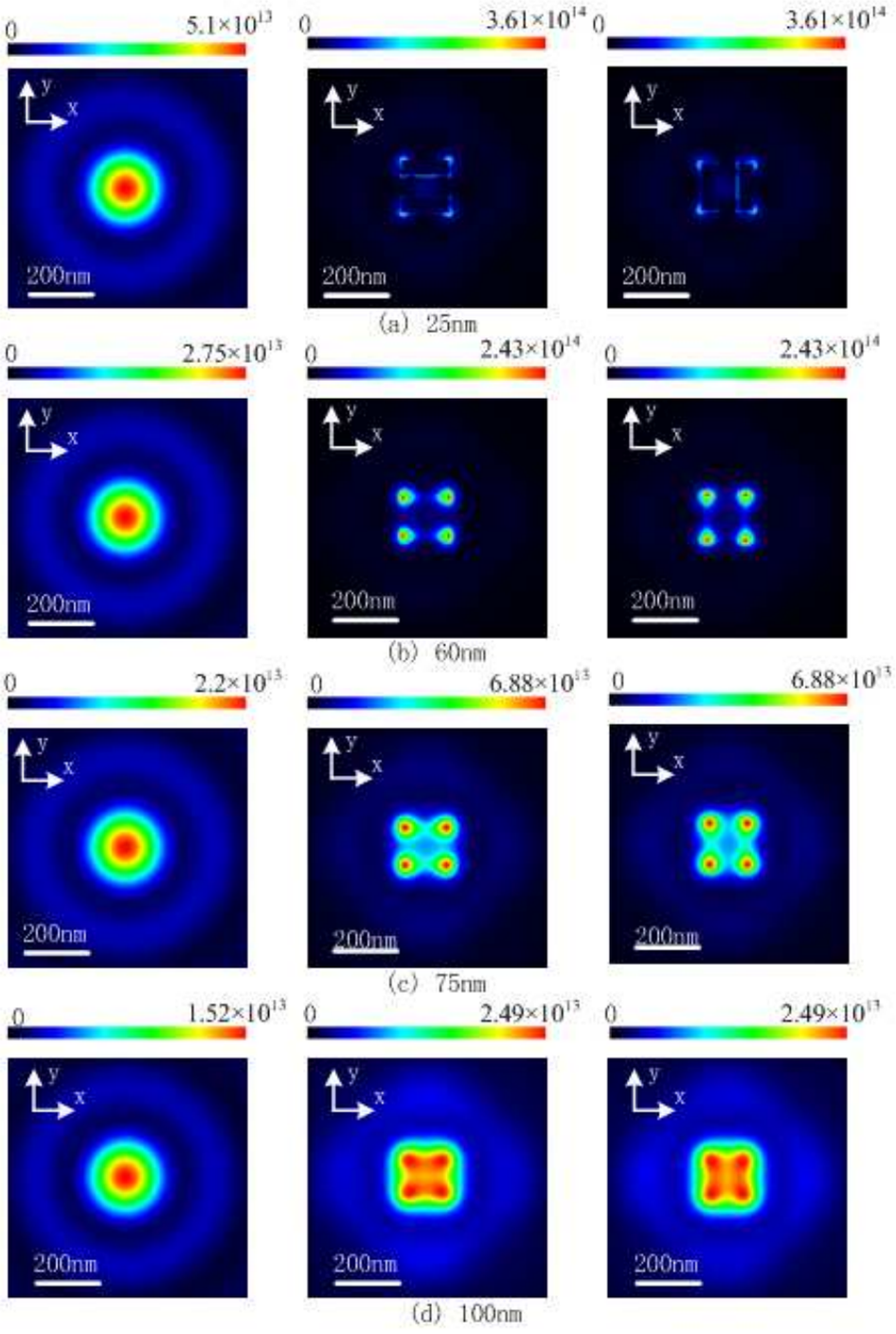

Figure 9. Intensity distributions for radially polarized focal beam in *xy* plane of different distances from the interface. In the left column there is no nanorod. In the middle column the nanorods are lying along *x* direction. In the right column the nanorods are lying along y direction. (Unit: V^2/m^2)

It is well known that the focal spot for radially polarized beam is circularly symmetrical. According to the analysis demonstrated in the previous section, it is expected that the circular symmetry would be broken due to the LSPs effect which is polarization sensitive. Fig.9 shows the intensity distributions of evanescent radially polarized focal beam at *xy*

planes of different distances above the interface for three cases, including without nanorods, nanorods lying in the x and y directions, respectively. The focal spot is circularly symmetrical and decay exponentially further from the interface without the presence of the nanorods, as shown in the left column of Fig.9. With strong LSPs effect from the nano-plasmonic waveguide, the circular symmetry is broken, and the focal spot shows a strong intensity lobe at each of the four ends of the two nanorods (Figs. 9 (b-d)). It is noted that the intensity of the longitudinal component E_z is approximately one order of magnitude stronger than that of the transverse components. As a result, the intensity distribution at the focal region shows four strong intensity lobes produced by LSPs effect excited by the longitudinal polarization component E_z.

In this section we demonstrate a new method to modulate highly focused evanescent field with a nano-plasmonic waveguide. The modulation of focus is based on the mechanism that the LSPs are polarization sensitive and the focus is strongly depolarized by a high numerical aperture objective. For a simple nano-plasmonic waveguide that consists of two silver nanorods lying on the interface between two dielectrics, LSPs effect is strongest for the polarization component perpendicular to the nano-plasmonic waveguide. A super-resolved focal spot with significantly enhanced strength can be achieved, when the nanorods are lying perpendicular to the dominant polarization component. The design of the nano-plasmonic waveguide structure gives rise to a new approach to further improve the tightly focused evanescent field to achieve the resolution beyond diffraction limit, and thus facilitates potential applications in nano-trapping and nano-lithography.

4. Plasmonic nano-waveguiding

In this section we will propose the waveguiding properties of two types of plasmonic nano-structures: parallel long nano-wires and the metal-dielectric-metal waveguide. They all present interesting optical nano-waveguiding properties and can be applied in some special research areas.

4.1. Focusing through parallel nanorods that perpendicular to the interface

In recent years, metallic nanorods are intensely investigated and widely applied in the field of super-long waveguiding [31]. It has been reported that the optical properties of single nanorod is sensitive to the polarization of incident wave and the rod aspect ratio [32]. While for the two parallel nanorods and U-shaped nanorods, their optical properties are more complicated and interesting [33]. The SPPs excited along the surface of single nanorod couple between the nanorods, which leads to the extinction spectrum whose resonance peaks are dependent on the geometry of the nanorods. The U-shaped nanorods show stronger resonance strength and more longitudinal couple modes than the two parallel nanorods.

In some cases, such as super-resolution imaging or focusing, the more complicated focusing beam with three polarization components should be considered as the incident source.

However, the interaction between the focal beam and the two nanorods has not been investigated thoroughly yet. Here we fist present the SPR excitation spectrums of two parallel silver nanorods and the π-shaped silver nanorods using the FDTD method. Second we simulate the focusing process through these two structures using 3D FDTD method, respectively. The waveguide effect and electromagnetic field transfer efficiency of these two structures are compared and analyzed. Finally, the focusing process through the angular π-shaped nanorods structure is simulated which presents the ability of guiding the focal field to different directions.

4.1.1. Simulation modeling and resonance spectrums

The schemes of two silver nanorods structures are shown in Fig.10. In Fig.10(a), the length of nanorods is *l*, the diameter of nanorods is *a* and the distance between the two nanorods is *d*. In Fig.10(b), the length of longitudinal nanorods is l_1, the length of transverse nanorod is l_2. In our simulations, we set a=50nm, l=l_1=500nm, and l_2=260nm constantly, and change the distance *d* from 30nm to 100nm gradually to calculate their SPR spectrums.

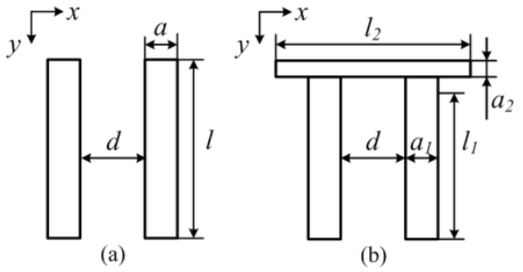

Figure 10. Structures of silver nanorods waveguide. (a) Two parallel nanorods structure; (b) π-shaped nanorods structure

An *x*-polarized Gaussian temporal profile pulse with the central wavelength of 400nm is injected from the upper side and propagates through the nano-structures. The spectrum width of the pulse is wide enough to cover the wavelength range from 300nm to 1000nm. The temporal electromagnetic field coupling between the nanorods at the central cross section of the nanorods is recorded, and transformed to frequency domain using Fourier transform, and divided by the incident wave magnitude at each wavelength component to calculate the enhancement coefficient spectrum.

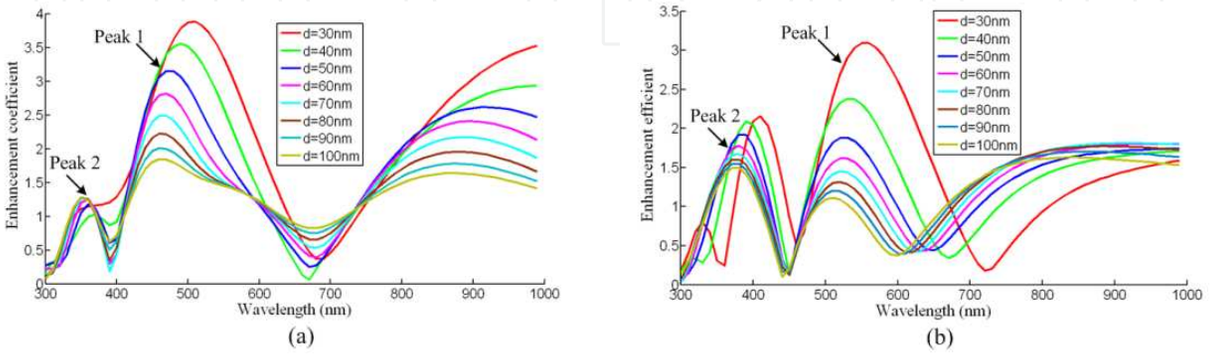

Figure 11. Electromagnetic field enhancement coefficient of the SPR coupling between the two silver nanorods. (a) Two parallel nanorods structure; (b) π-shaped nanorods structure.

As shown in Fig.11, the spectrums perform two peaks for both structures, but the positions of the peaks of the two structures under the same distance d are different. In Fig.11(a), for the two parallel nanorods structure, the main resonance peak 1 shows blue shift with the increase of the distance d, while the sub-resonance peak 2 remains at the wavelength about 350nm. In Fig. 11(b), the main resonance peak 1 also shows blue shift with the increase of the distance d. The peak 2 remains at about 390nm but becomes stronger. Due to the reflection by the transverse nanorod in the π-shaped nanorods structure, their enhancement coefficients are a little smaller than those of the two parallel nanorods structure.

4.1.2. Focusing through nanorods structures

Based on the results obtained above, we will investigate the focusing processes through the nanorods structures in this section. Due to the depolarization effect of high numerical aperture objective, the incident linearly polarized beam would change its polarization state after propagating through the objective, i.e. the strong longitudinal polarization component occurs. The interaction effect between the incident focal beam and the two nanorods structures are more complicated than that of the single polarized incident beam case. Here the focal beam is calculated by the vectorial Debye theory and induced into the 3D FDTD simulation region with total-field/scatter-field method. The refractive index of upper medium is 1.78 and the refractive index of lower medium is 1.0. The numerical aperture of the objective is 1.65, and the pure focused evanescent field is generated by inserting a centrally placed obstruction disk with the normalized radius ε_c=0.606, corresponding to the total internal refraction condition at the interface between the two media. We fix the distance d=70nm throughout the following simulations, so that the tops of the two parallel nanorods are all covered in the focal region. The wavelength of focal beam is 532nm which corresponding to the resonance peak of π-shaped nanorods structure at d=70nm condition. We place the nanorods structures normally onto the interface, and set the length of the longitudinal parallel nanorods to 1250nm to observe the long waveguide effect for transferring the electromagnetic field from the focus region to the far field. The 3D discretized cell sizes for three directions are Δx=Δy=Δz=4.68nm and the time step Δt=8.27288e-18s which satisfies the Courant stability condition. After 4000 time steps simulation, the total electromagnetic field is stable and the time averaged intensity distributions are obtained as shown in Fig.12.

The long waveguide effect produced by the nanorods structures are clearly shown in Fig.12. Without the nano-structures, the pure evanescent focal field would decay exponentially away from the interface and only can propagate no more than 100nm. However, when the nanorods structures are implemented onto the interface, the SPPs are excited by the evanescent focal field along the surfaces of the nanorods. The electromagnetic fields along the inner surface of the longitudinal nanorods are stronger than those along the outer surface of the longitudinal nanorods, which means that the SPPs between the two nanorods couple with each other and form a long waveguide. The SPPs propagate along the nanorods with a resonance mode, with each space resonance period about 150nm in length. The electromagnetic field can be transferred to the lower end of the nanorods where is the far field more than 1μm.

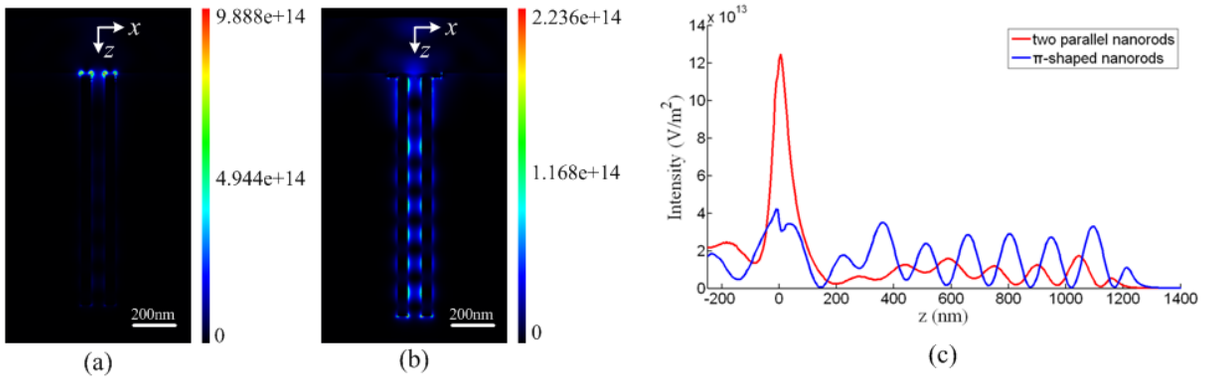

Figure 12. Focusing through long nanostructure waveguide. (a) Two parallel nanorods structure; (b) π-shaped nanorods structure; (c) Plot of intensity along the z axis. Color bar unit: V^2/m^2.

The two parallel nanorods structure and the π-shaped nanorods structure show almost the same SPPs resonance mode, except their excitation strength. In Fig.12(a), the electromagnetic field is strongly enhanced at the top of the two nanorods and decay exponentially very fast, which leads to four strong field points at the top of the nanorods. In Fig.12(b), the focal field is evenly enhanced by the transverse nanorod, so there is no strong field point shown at the top side. The comparison of the electromagnetic field intensities along *z* axis of the two situations is shown in Fig.12(c). At the interface of the two media(0 position along *z* axis), the two parallel nanorods show stronger intensity than the π-shaped nanorods. However, at the distances larger than 200*nm* along *z* axis, the π-shaped nanorods show stronger intensity than the two parallel nanorods. There are two reasons for this phenomenon. First, under *d*=70*nm* condition, the incident wavelength 532*nm* is almost the SPR wavelength for the π-shaped nanorods structure as shown in Fig.11(b), but not the SPR wavelength for the two parallel nanorods structure as shown in Fig.11(a). Second, the transverse nanorod of π-shaped nanorods interacts with the longitudinal polarization component of the focal beam, so that the longitudinal SPPs along the surfaces of the nanorods are excited, which gives contribution to the total SPPs intensity in the nanorods waveguide. The π-shaped nanorods structure shows stronger electromagnetic field enhancement and better energy transfer efficiency in the far field than the two parallel nanorods structure. This result gives a method to transfer the focal field from the focus region to the far field.

Finally, we present the simulation of focusing through the angular π-shaped nanorods structure as shown in Fig.13(a). The two legs of the π-shaped nanorods are bent by the angle of 90°, so that the ends of the nanorods shift from the optical axis with the distance of l_2. In our simulation, we set l_1=500*nm*, l_2=500*nm*, l_3=260*nm*, *d*=70*nm* and *a*=50*nm*. The incident wavelength keeps 532*nm*. The simulation results for different cross section planes are shown in Fig.13(b), (c) and (d). In Fig.13(b), the intensity distribution in the *xz* plane shows the same pattern with that in Fig.12(b). In Fig.13(c), the intensity distribution in the *yz* plane shows an "L" shaped optical path which formed by the SPPs coupled between the two nanorods. This phenomenon testifies that the SPPs can propagate not only along the straight path, but also along the angular path with the angular structure of the nanorods. The focal electromagnetic field can be transferred not only along the optical axis, but also to the

directions that perpendicular to the optical axis. In Fig.13(d), the xy plane is the cross section through the centers of the lower two transverse nanorods. It shows the same resonance length with the longitudinal part of the waveguide. It can be predicted that if we change the bend angle to other degrees, the SPPs also can be transferred to other directions. Due to the limit memory of computer, we can't simulate the waveguiding effect of longer nanorods structures, but it can be seen that the electromagnetic field waveguiding ability of the two nanorods structures investigated in this paper must be far more than $1\mu m$.

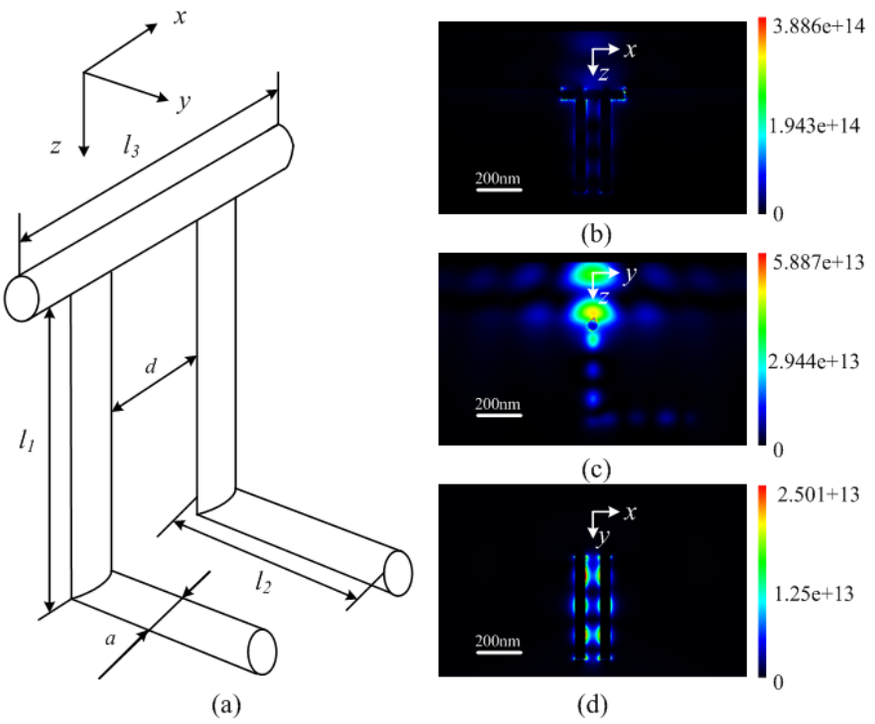

Figure 13. Focusing through angular π-shaped nanorods structure. (a) The configuration of the angular π-shaped nanorods structure; (b) The intensity distribution in xz plane; (c) The intensity distribution in yz plane.

In this section, the optical properties of two silver nanorods plasmonic waveguide structures are simulated with the FDTD method. The SPR spectrums of the two parallel nanorods and the π-shaped nanorods structures are calculated, which show different SPR resonance peaks at the same distance condition for both structures. The focusing processes through these two types of structures show almost the same SPPs resonance mode with each resonance period about $150nm$. However, at the far field, the electromagnetic field enhancement of the π-shaped nanorods structure is stronger than that of the two parallel nanorods, due to the contribution of longitudinal SPPs component excited by the transverse nanorod. At last, the focusing process through the angular π-shaped nanorods structure indicates that the focus field can be transferred not only to the far field along the optical axis, but also to any other directions that the ends of the two nanorods direct to. The two nanorods plasmonic waveguide structures studied in this paper have potential applications in nano-biosensing, nano-trapping or nano-waveguiding.

4.2. MDM nano-waveguides

Plasmonic waveguides based on the principles of SPPs have gained great attentions in recent years due to their ability of confining and guiding optical field in sub-wavelength scale. Among various types of plasmonic waveguides, the metal-dielectric-metal (MDM) waveguide is considered to be a key element in the fields of waveguide couplers[34, 35], sub-wavelength scale light confinement[36, 37], wavelength filters[38] and integrated optical devices[39, 40]. The remarkable advantages of the MDM waveguide, including the strong confinement of optical field in nano-scale gaps, the high sensitivity of its transmission characteristics to the waveguide structures, and the facility of its fabrication, attracted a great deal of effort to be devoted to develop the MDM based nano-plasmonic devices. It has been reported that the transmission of MDM waveguide coupled with stub structure could be changed with the length of the stub[38]. Further more, the stub filled with absorptive medium was considered to be a resonance cavity that acts as an optical switch controlled by the pumping field[39]. An improved transmission model[40] was also developed to describe the transmittance of multi-stubs MDM structure.

The investigation approaches for the transmission characteristics of MDM waveguide include theoretical transmission line theory(TLT) and FDTD method [40]. In this section, we first provide the formulas of the optical transmission characteristics of the MDM waveguide with a stub structure deduced by TLT. And then the FDTD method will be employed to numerically study the optical switch effect of the stub structure in terms of changing the length and the refractive index of the stub, respectively. The simulation results coincide with the calculation results of TLT and the physical mechanisms of the optical switch effect are analyzed and discussed.

4.2.1. Scheme modeling and transmission line theory

The scheme of the MDM waveguide coupled with a single stub structure is shown in Fig.14(a). Firstly we assume that the medium in the stub is air, i.e. $n_1=n_2=1.0$. The silver is employed as the dispersive medium for the MDM waveguide. The width of the waveguide and the stub is $d=100nm$. A transverse electric (TE) plane wave with a wavelength $\lambda=600nm$ is incident from the left side into the waveguide. The transmission line modeling of the schematic is shown in Fig.14(b).

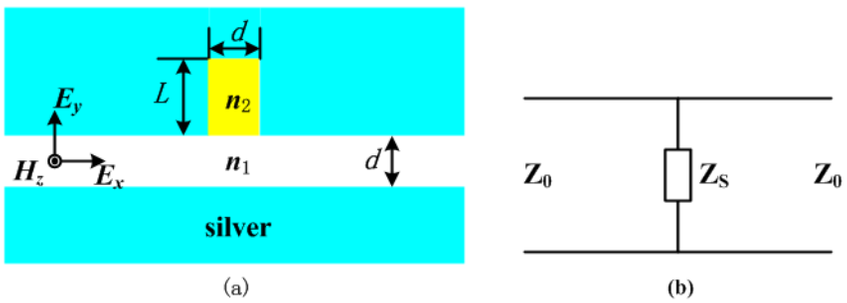

Figure 14. (a) The scheme of MDM waveguide coupled with a stub structure with the same width d and the length L. (b) The transmission line modeling of the scheme.

According to the transmission line theory, the stub can be considered as admittance. Assume that the phase shift only occurs when the SPPs are reflected by the end of the stub. Z_0 and Z_s are the characteristic impedances of the loss-free transmission lines corresponding to the MDM waveguide and the stub[40], respectively. Their relation is expressed as:

$$\frac{1}{Z_s} = -j\frac{1}{Z_0}\tan\left(\frac{2\pi L}{\lambda_{SP}}\right) \tag{27}$$

where L is the length of the stub and λ_{SP} is the propagating wavelength of the SPPs. From Fig.14(b), the amplitude transmission of the electric field can be expressed as:

$$t = \frac{2Y_0}{2Y_0+Y_s} \tag{28}$$

where $Y_0=1/Z_0$ and $Y_S=1/Z_S$. Therefore, the energy transmission of the MDM waveguide coupled with a single stub is finally expressed as[38]:

$$T = \frac{4}{4+\tan^2\left(\frac{2\pi L}{\lambda_{SP}}\right)} \tag{29}$$

From Equ.(29) we can see that the energy transmission is the function of L and λ_{SP}. In the stub, the SPPs wavelength λSPS can be changed by the refractive index of the medium in the stub. As a result, the transmission would be modulated periodically by changing the length L and the refractive index n_2 of the stub linearly.

4.2.2. Numerical simulation modeling and results

We simulated the transmission of the MDM waveguide with L ranging from 0 to 1μm by 2D FDTD algorithm. The relative permittivity of silver is described by Drude-Lorentz model to fit the experimental data of relative permittivity of silver and implemented into FDTD program with the PLRC method. The discretized cell size is $\Delta x=\Delta y=5nm$. After 3000 time steps simulation, the results are shown in Fig.15.

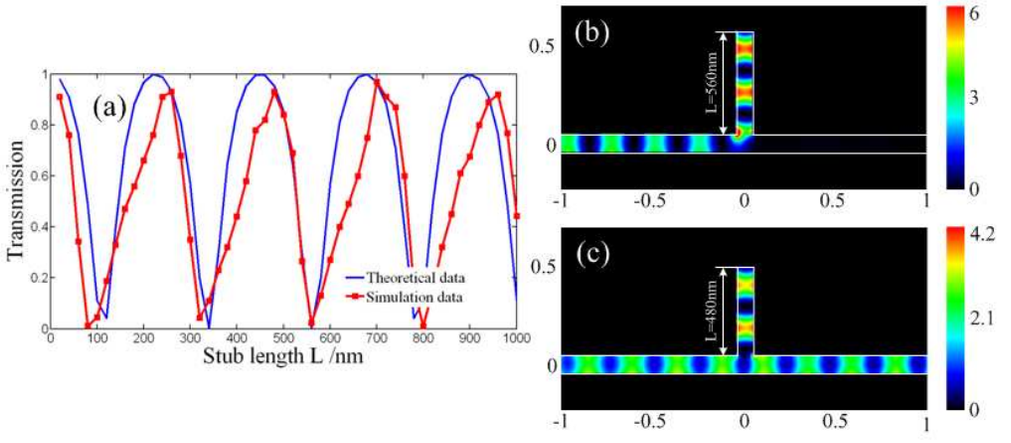

Figure 15. The transmission of MDM waveguide coupled with a stub structure as a function of the stub length. (a) Compare of the transmission calculated by transmission line theory and FDTD simulation. (b) The intensity distribution of the MDM waveguide at the "off" state with L=560nm. (c) The intensity distribution of the MDM waveguide at the "on" state with L=480nm.

From Fig.15(a) we can see that the simulation results agree well with the theoretical data calculated by Equ.(29). The SPPs excited along the surfaces of the metal layers propagate in the waveguide with a resonance mode. When passing through the stub, a part of the SPPs propagate into the side-coupled stub. The SPPs reflected from the end of the stub interfere with the passing SPPs, which leads to a modulation of the superposition wave. If we change the length of the stub, the phase change of the interference would cause the transmission vary from 0 to 1, so that the MDM waveguide coupled with a single stub structure presents the optical switch effect on the incident wave. As the incident wavelength λ=600nm, the λ_{SP} is approximately to be 480nm. The transmission shows about 4.5 periods for L linearly ranging from 0 to 1μm in length. The lowest transmissions are less than 1%, and the highest transmissions are more than 92%, which means the transmission of this structure switches between "on" and "off" states with the variation of the length of the stub. As shown in Fig.15(b), when the transmission is at the "off" state with L=560nm, the reflected light from the end of the stub modulates the interference intensity to be 0, which causes the propagating SPPs in the waveguide stopped by the stub significantly. As shown in Fig. 15(c), when the transmission is at the "on" state with L= 480nm, the SPPs can be transferred to the end of the waveguide without any loss. For both states, the superposition of the waves going into the stub and reflected by the end of the stub makes the field intensity in the stub stronger than that in the waveguide. Moreover, the field intensity of "off" state is stronger than that of "on" state due to the storage of the stopped field energy in the stub by the interference.

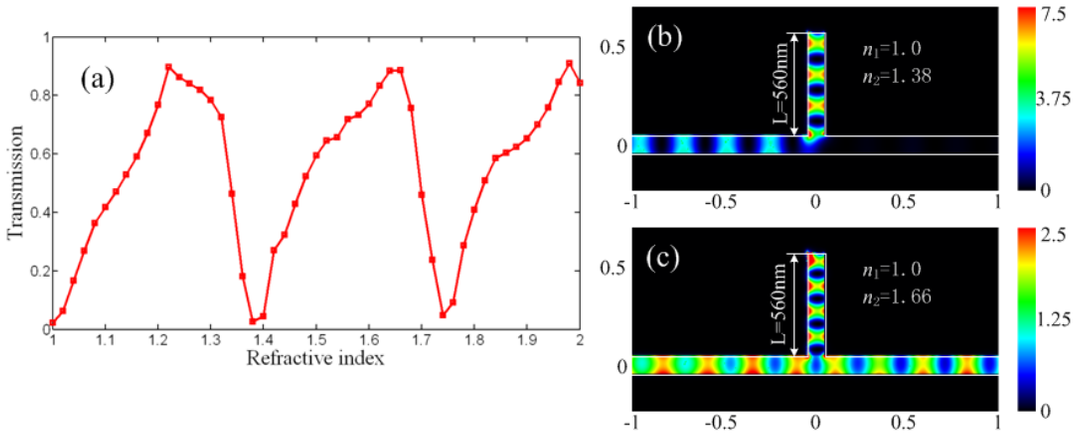

Figure 16. (a)The transmission of the MDM waveguide coupled with a stub structure as a function of the refractive index n_2 of the stub. (b) The "off" state when n_2=1.38. (c) The "on" state when n_2=1.66.

Another approach for modulating the phase of the reflected wave from the end of the stub is changing the refractive index of the stub. We carried out a series of simulations with the refractive index n_2 ranging from 1.0 to 2.0, and keeping n_1=1.0. The simulation results are shown in Fig.16. In Fig.16(a), it is obviously that the transmission demonstrate a periodic distribution as a function of the refractive index n_2. This phenomenon is similar with the distribution as shown in Fig.15(a). The mismatch of n_1 and n_2 leads to the phase difference between the reflected wave in the stub and the passing wave in the waveguide which also processes a phase modulation effect for the interference wave. Fig.16(b) and (c) show the

phenomena of "off" and "on" states of the transmission when n_2=1.38 and n_2=1.66, respectively. It is clearly shown that the effective wavelength of the propagating SPPs in the stub is changed according to the refractive index n_2. The field intensity at "off" state is also much higher than that at "on" state because of the storage of the SPPs energy in the stub.

We have numerically studied the transmission characteristics of the MDM waveguide coupled with stub structure as functions of the length and the refractive index of the stub, respectively. The 2D FDTD simulation results show that the transmission rates obtained by both approaches change as periodical distributions, which implies that the MDM waveguide can be treated as an optical switch device controlled by the length and the refractive index of the stub. The physical mechanism of this phenomenon is the phase modulation of the interference of the reflected SPPs wave from the end of the stub and the passing SPPs wave in the waveguide. The results help us to further apply the MDM waveguide as an optical switch element in nano-scale optical chips and optical integrated devices.

5. Conclusions

The importance of surface plasmons in the applications of nano-photonics has been proved in many examples. In this chapter we focused on two fields: super-resolution focusing and nano-waveguiding. Super-resolution focusing is the key element for nano-lithography, high density optical data storage, and super-resolution imaging. We have presented that the high density focal field can be re-distributed by some specified metallic nano-structures such as nano-film and parallel nanorods, so that a super-resolution focusing can be generated in some particular space areas. This method can be further applied in optical nano-trapping due to the small and enhanced plasmonic focus. While for nano-waveguiding there have been many nano-structures and methods reported previously. Here we have presented the parallel nanorods and MDM structures, respectively. When the parallel nanorods are perpendicularly put on the interface of two materials, the incident focal field generates surface plasmons along their surfaces which form a nano-waveguide. The fields of focus can propagate along the waveguide for a long distance. The MDM with a stub structure showed a optical switch effect with the altering of the length and the refractive index of the stub, which has a potential application in optical communications and optical sensing.

Author details

Xingyu Gao
Institute of Opto-mechatronics, Guangxi Key Laboratory of Manufacturing System & Advanced Manufacturing Technology, School of Mechanical & Electrical Engineering, Guilin University of Electronic Technology, Guilin Guangxi, China

6. References

[1] William L.Barnes, Alain Dereux and Thomas W. Ebbesen. Surface plasmon subwavelength optics. Nature 2003; 424(6950) 824-830.

[2] R.H.Ritchie. Plasma Losses by Fast Electrons in Thin Film. Phys. Rev. 1957; 106(5) 874-881.
[3] Hiroshi Kano, Seiji Mizuguchi, and Satoshi Kawata, Excitation of surface-plasmon polaritons by a focused laser beam, J. Opt. Soc. Am. B 1998; 15(4) 1381-1386.
[4] Lihong Shi and Lei Gao. Subwavelength imaging from a multilayered structure containing interleaved nonspherical metal-dielectric composites. Phys. Rev. B 2008; 77(19) 195121.
[5] Thierry Laroche and Christian Girard. Near-field optical properties of single plasmonic nanowire. Appl. Phy. Lett. 2006; 89(23) 233119.
[6] Stephen K. Gray and Teobald Kupka. Propagation of light in metallic nanowire arrays: Finite-difference time-domain studies of silver cylinders. Phy. Rev. B 2003; 68(4) 045415.
[7] Yuan-Fong Chao, Min Wei Chen and Din Ping Tsai. Three-dimensional analysis of surface plasmon resonance models on a gold nanorod. Appl. Opt. 2009; 48(3) 617-622.
[8] Xingyu Gao and Xiaosong Gan. Modulation of evanescent focus by localized surface plasmons waveguide. Opt. Express 2009; 17(25) 22726-22734.
[9] Fu Min Huang, Nikolay Zheludev, Yifang Chen, et al.. Focusing of light by a nanohole array. Appl. Phy. Lett. 2007; 90(9) 091119.
[10] Yakov M. Strelniker. Theory of optical transmission through elliptical nanohole arrays. Phy. Rev. B 2007; 76(8) 085409.
[11] Haofei Shi, Changtao Wang, Chunlei Du, et al. Beam manipulating by metallic nano-slits with variant widths. Opt. Express 2005; 13(18) 6815-6820.
[12] Michael G. Somekh, Shugang Liu, Tzvetan S. Velinov, et al. High-resolution scanning surface-plasmon microscopy. Appl. Opt. 2000; 39(34) 6279-6287.
[13] Maurizio Righini, Giovanni Volpe, Christian Girard, et al. Surface Plasmon Optical Tweezers: Tunable Optical Manipulation in the Femtonewton Range. Phy. Rew. Lett. 2008; 100(18) 186804.
[14] Patrick Englebienne, Anne Van Hoonacker and Michel Verhas. Surface plasmon resonance: principles, methods and applications in biomedical sciences. Spectroscopy, 2003; 17: 255~273.
[15] Jason M. Montgomery and Stephen K. Gray. Enhancing surface plasmon polariton propagation lengths via coupling to asymmetric waveguide structures. Phys. Rev. B 2008; 77(12) 125407.
[16] K.S.Yee. Numerical Solution of Initial Boundary Value Problems Involving Maxiwell's Equations in Isotropic Media. IEEE Trans. Antennas Propagat. 1966; 14(3) 802-807.
[17] A. Taflove and S. C. Hagness. Computational Electrodynamics: The Finite-Difference Time-Domain Method. 3rd ed, Norwood, MA: Artech House; 2005.
[18] Raymond J. Luebbers, Forrest P. Hunsberger, Karl S. Kunz, et al. A Frequency-Dependent Finite-Difference Time-Domain Formulation for Dispersive Materials. IEEE Trans. Electromag. Compat. 1990; 32(3) 222-227.
[19] Rose M. Joseph, Susan C. Hagness, and Allen Taflove. Direct time integration of Maxwell's equations in linear dispersive media with absorption for scattering and propagation of femtosecond electromagnetic pulses. Opt. Lett. 1991; 16(8) 1412-1414.

[20] Dennis M. Sullivan. Frequency-Dependent FDTD Methods Using Z Transforms. IEEE Trans. Antennas Propag. 1992; 40(10) 1223-1230.
[21] Ge Debiao, Wu Yueli, Zhu Xiangqin. Shift operator method applied for dispersive medium. Chinese J. Radio Sci. 2003; 18(4) 359-362.
[22] David F. Kelley and Raymond J. Luebbers. Piecewise Linear Recursive Convolution for Dispersive Media Using FDTD. IEEE Trans. Antennas Propag. 1996; 44(6) 792-797.
[23] Jun SHibayama, Taichi Takeuchi, Naoki Goto, et al. Numerical Investigation of a Kretschmann-Type Surface Plasmon Resonance Waveguide Sensor. J. Lightw. Technol. 2007; 25(9) 2605-2611.
[24] Xingyu Gao, Zexin Xiao, Lihua Ning. Surface plasmon enhanced super-resolution focusing of radially polarized beam. OSA-IEEE Topical Conference: Advances in Optoelectronics & Micro/nano-Optics. 2010:5713551.
[25] P.B. Johnson and R. W. Christy. Optical Constants of the Noble Metals. Phys. Rew. B 1972; 6(12) 4370-4397.
[26] James W. M. Chon and Min Gu. Scanning total internal reflection fluorescence microscopy under one-photon and two-photon excitation: image formation. Appl. Opt. 2004; 43(5) 1063-1071.
[27] Baohua Jia, Xiaosong Gan, and Min Gu. "Direct measurement of a radially polarized focused evanescent field facilitated by a single LCD," Opt. Express 13, 6821-6827.
[28] Baohua Jia, Xiaosong Gan, and Min Gu. Direct measurement of a radially polarized focused evanescent field facilitated by a single LCD. Opt. Express 2005; 13(18) 6821-6827.
[29] A. Husakou and J. Herrmann. Subdiffraction focusing of scanning beams by a negative-refraction layer combined with a nonlinear layer. Opt. Express 2006; 14(23) 11194-11203.
[30] A. Husakou and J. Herrmann. Focusing of Scanning Light Beams below the Diffraction Limit without Near-Field Spatial Control Using a Saturable Absorber and a Negative-Refraction Material. Phy. Rev. Lett. 2006; 96(1) 013902.
[31] R. F. Oulton, V. J. Sorger, D. A. Genov, et al. A hybrid plasmonc waveguide for subwavelength confinement and long-range propagation. Nature Photonics 2008; 2(8) 496-500.
[32] Yuan-Fong Chau, Din Ping Tsai, Guang-Wei Hu, et al. Subwavelength optical imaging throught a silver nanorod. Opt. Eng., 2007; 46(3) 039701.
[33] Zhongyue Zhang and Yiping Zhao. Optical properties of U-shaped Ag nanostructures. J. Phy: Condens. Matter 2008; 20(34) 345223.
[34] G. Veronis and S. Fan. Subwavelength light bending by metal slit strctures. Opt. Express 2005; 13(24) 9652-9659.
[35] R. A. Wahsheh, Z. Lu and M. A. G. Abushagur. Nanoplasmonic couplers and splitters. Opt. Express 2009; 17(21) 19033-19040.
[36] Ki Young Kim, Young Ki Cho, and Heung-Sik Tae. Light transmission along dispersive plasmonic gap and its subwavelength guidance characteristics. Opt. Express 2006; 14(1) 320-330.

[37] Y. C. Jun, R. D. Kekatpure, J. S. White, and M. L. Brongersma. Nonresonant enhancement of spontaneous emission in metal-dielectric-metal plasmon waveguide structures. Phy. Rev. B 2008; 78(17) 153111.

[38] Changjun Min and Georgios Veronis. Absorption switches in metal-dielectric-metal plasmonic waveguides. Opt. Express 2009; 17(13) 10757-10766.

[39] A. Pannipitiya, I. D. Rukhlenko, M. Premaratne, H. T. Hattori, and G. P. Agrawal. Improved transmission model for metal-dielectric-metal plasmonic waveguides with stub structure. Opt. Express 2010; 18(6) 6191-6204.

[40] Georgios Veronis, Zongfu Yu, Şükrü Ekin Kocabaş, David A. B. Miller, Mark L. Brongersma, and Shanhui Fan. Metal-dielectric-metal plasmonic waveguide devices for manipulating light at the nanoscale. Chin. Opt. Lett. 2009; 7(4) 302-308.